Automated detection of arterial wall boundaries based on correlation between adjacent

receive scan lines for elasticity imaging

Automated detection of arterial wall boundaries based on correlation between adjacent receive scan lines for elasticity imaging

Yukiya Miyachi[1,2], Hideyuki Hasegawa[2,3], and Hiroshi Kanai[3,2*]

[1]*Medical Systems Research and Development Center R&D Management Headquarters, FUJIFILM Corporation, Kaisei, Kanagawa 258-8538, Japan*
[2]*Graduate School of Biomedical Engineering, Tohoku University, Sendai 980-8579, Japan*
[3]*Graduate School of Engineering, Tohoku University, Sendai 980-8579, Japan*
E-mail: yukiya.miyachi@fujifilm.com

In our series of studies on the ultrasonic assessment of the regional elasticity of the arterial wall, the change in the thickness of the arterial wall caused by the heartbeat was measured by the ultrasonic phased-tracking method. In the measurement of elasticity, the boundaries of the anterior and posterior walls must be assigned in advance. Currently the boundaries are manually determined by the operator, which is time-consuming and results in observer variability. In this paper, we propose an automated method for the detection of arterial wall boundaries using multiscale dynamic programming, in which the cost function includes the correlation term between ultrasonic echoes in adjacent receive scan lines. The correlation term enables boundary detection that is more robust than conventional methods against noises. The effectiveness of the proposed method was validated using a phantom and applied to the in vivo measurements of carotid arteries. The root mean square error between the results obtained by the proposed method and the manual assignment of the boundaries was significantly improved. © 2015 The Japan Society of Applied Physics

1. Introduction

Along with the recent changes in lifestyle in Japan, the incidence of coronary artery disease has increased.[1] Atherosclerosis has been considered to be the main cause of coronary artery disease and cerebral infraction. Because there are significant differences in elasticity between normal and atherosclerotic arterial walls,[2,3] the evaluation of arterial wall elasticity is useful.[4] Some markers that can be noninvasively measured for the detection of atherosclerosis have been identified, such as intima–media thickness (IMT) of the arterial wall, pulse wave velocity (PWV), and elasticity of the arterial wall.

Noninvasive ultrasonic B-mode imaging, where the amplitudes of received ultrasonic echoes are converted to brightness, is an important method for studying the progression and regression of atherosclerotic lesions in the carotid artery.[5–7] IMT is measured accurately from a B-mode ultrasonic image and studies for more accurate measurement of IMT have been conducted.[8–12] This measurement is used as a sensitive indicator of atherosclerosis in population-based studies. However, a conventional B-mode ultrasonic image provides only information on shape, and mechanical properties such as elasticity cannot be evaluated.

The PWV method has been developed to measure the elasticity of the arterial wall.[13–15] Propagation of the pressure wave along the arterial tree is evaluated in this noninvasive diagnostic method. Although it is useful for evaluation of global elasticity such as from the heart to the femoral artery, regional elasticity cannot be evaluated.

In a series of studies of Kanai and coworkers,[16–29] the elasticity of a local region has been evaluated by the ultrasonic phased-tracking method. In this method, a small change in the thickness of the arterial wall due to the heartbeat was accurately measured in each local region. From the measured changes in thickness and blood pressure, the regional elasticity of the arterial wall was evaluated noninvasively.

In the measurement of the elasticity of the arterial wall by this method, the boundaries of the arterial wall, between which the elastic modulus is calculated, must be configured beforehand. Currently, the media–adventitia and lumen–intima boundaries of the anterior and posterior arterial walls are manually determined by the operator. Since the manual configuration of the boundaries is time-consuming and results in inter- and intra-observer variabilities, a fast automated method is necessary for the detection of the boundaries.

In previous research, efforts to detect the boundaries have been made by investigators worldwide. Touboul et al. in 1992 reported that IMT was automatically computed as the distance between midpoints of the rising slopes of the two pulses from the lumen–intima and media–adventitia boundaries.[30] In 1993, Gariepy et al. presented a system with which the lumen–intima and media adventitia boundaries are detected from changes in intensity based on default positions that are traced by an operator.[31] Selzer et al. in 1994 described a three-step method as follows: (1) approximate echo boundaries are identified manually; (2) the approximate boundaries are used to guide the edge-finding algorithm; (3) the initial edges are tested in terms of edge strength, and weak edges are eliminated.[32] Beux et al. also used the gradient of the intensity in the B-mode image of the artery.[33]

The above methods all required a default setting by a human operator, which could bring variability owing to subjective judgment. The above algorithms are based on the evaluation of local features in a single image, either the intensity or the intensity gradient. These methods can detect boundaries precisely if a B-mode image is clear. Unfortunately, most B-mode images in a clinical situation contain various types of noise such as speckle noise and multiple reflection noise, making it difficult to detect the boundaries precisely. Several methods using a cost function have been proposed for the detection of the boundaries, which are robust against noise.[34–40] Among these methods, Liang et al. proposed a fully automated method using multiscale dynamic programming (DP), in which the cost function is composed of echo intensity, echo intensity gradient, and change in vertical distance.[36]

In this paper, we propose an automated method for the detection of arterial wall boundaries using multiscale DP for automated measurement of elasticity, in which the correlation between ultrasonic echoes in adjacent receive scan lines is added to the cost function as a new feature. The correlation
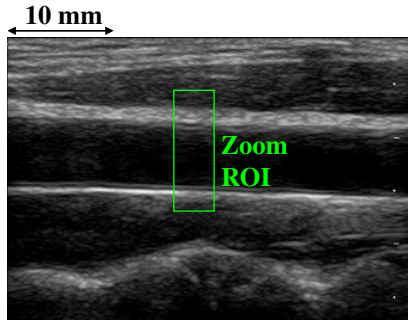
Fig. 1. (Color online) Carotid artery B-mode image.

Fig. 2. (Color online) Procedure for measuring the elasticity of the arterial wall. (a) Zoomed B-mode image of carotid artery with manually traced boundaries overlaid. (b) M-mode image in the red line in (a) with anterior and posterior wall boundary tracking results overlaid. (c) Elasticity image.

term enables more robust boundary detection to various types of noise. Also, this method is used for the automated detection of cardiac cycles, which is indispensable for the automated measurement of elasticity. The effectiveness of the proposed method is validated using a phantom and applied to the in vivo measurement of carotid arteries.

2. Principles

2.1 Elasticity imaging method

To show the need for automated boundary detection, manual trace processing for assessment of the elasticity of the carotid arterial wall is shown in this section. The displacement of an object is estimated from the quadrature demodulated signal of the received ultrasonic RF echoes. Experiments were conducted using ultrasonic diagnostic equipment, FUJIFILM FAZONE M and an L10-5 linear type probe (with a frequency range from 5 to 10 MHz). The quadrature demodulated signal was saved by a research data acquisition tool named "IQscan".[41]

As shown in Fig. 1, a B-mode image of the carotid artery is zoomed to obtain a high frame rate of 200 Hz for acquisition of quadr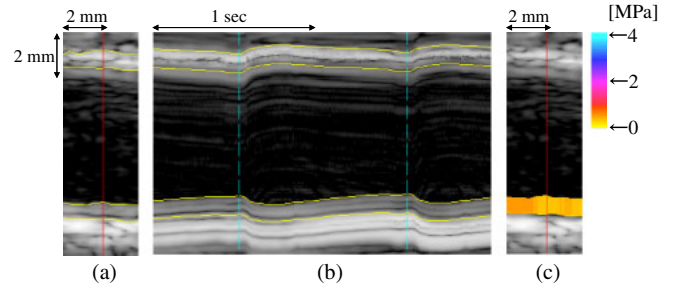ature demodulated signals. The typical zoom image size is 4 mm in width, 12 mm in height. The sampling interval of the quadrature demodulated signal and the pitch of scan lines were 0.035 and 0.12 mm, respectively. For the zoomed image, the lumen–intima and media adventitia boundaries of the anterior and posterior walls are manually assigned. To reduce tracking error, an image frame used for manual tracing is chosen close before the timing of the minimum diameter. Figure 2(a) shows the zoomed B-mode image of the carotid artery with manually traced boundaries overlaid.

With respect to N_l sampled points between the assigned lumen–intima boundary and the media–adventitia boundary along the l-th ultrasonic beam, the displacement of each point, $x_i(t; l)$ ($i = 1, 2, \ldots, N_l$), is estimated using the phased-tracking method.[16] For estimation of the displacement, using the quadrature demodulated signal $z(t; d; l)$ reflected at the time t, at the depth d along the l-th ultrasonic beam, the phase shift $\Delta\Psi_i(t; l)$ between echoes in two consecutive frames is obtained from the complex cross-correlation function as follows:

$$\exp[j\Delta\hat{\psi}_i(t; l)] = \frac{\sum_{m=-M_{\mathrm{C}}/2}^{M_{\mathrm{C}}/2} z(t + T_{\mathrm{r}}; d + x_i(t; l) + mD; l) \cdot z^*(t; d + x_i(t; l) + mD; l)}{\left| \sum_{m=-M_{\mathrm{C}}/2}^{M_{\mathrm{C}}/2} z(t + T_{\mathrm{r}}; d + x_i(t; l) + mD; l) \cdot z^*(t; d + x_i(t; l) + mD; l) \right|}, \tag{1}$$

where D and T_{r} are the interval of sampled points in the depth direction and the pulse repetition interval, respectively, and $*$ represents the complex conjugate. In Eq. (1), the number of sampled points, $M_{\mathrm{c}} + 1$, is set at 9 ($= 0.41\,\mu\mathrm{s}$) in consideration of the pulse length of $0.45\,\mu\mathrm{s}$. In estimation of the phase shift by Eq. (1), the object position is tracked by integration of the average velocity $v_i(t + T_{\mathrm{r}}/2; l)$ during the pulse repetition interval T_{r} as follows:

$$\hat{x}_i(t + T_{\mathrm{r}}; l) = \hat{x}_i(t; l) + \hat{v}_i\left(t + \frac{T_{\mathrm{r}}}{2}; l\right) \times T_{\mathrm{r}}$$

$$= \hat{x}_i(t; l) + \frac{c_0}{2\omega_0}\Delta\hat{\psi}_i(t; l) \times T_{\mathrm{r}}, \tag{2}$$

where ω_0 and c_0 are the center angular frequency of the ultrasonic pulse and the speed of sound, respectively. Figure 2(b) shows the M-mode image in the red line on Fig. 2(a) with tracking results for the anterior and posterior wall boundaries overlaid.

From the displacement $x_i(t; l)$ estimated during the repetition interval T_{r}, which are set at the i-th point in the arterial wall along the l-th ultrasonic beam, the small change in the thickness $\Delta h_i(t; l)$ of the arterial wall is obtained as follows:

$$\Delta h_i(t; l) = x_i(t; l) - x_{i+1}(t; l)$$

$$= \int_0^t [v_i(t; l) - v_{i+1}(t; l)]\, dt. \tag{3}$$

From the ratio of the maximum decrease in thickness during a cardiac cycle, $\Delta h_{i,\max}(l) = \max_t |\Delta h_i(t; l)|$, to the initial thickness, $h_0(l)$, of the i-th layer, the maximum strain of the i-th layer is obtained by $\Delta\varepsilon_{i,\max}(l) = \Delta h_{i,\max}(l)/h_0(l)$.

By assuming that the arterial wall is incompressible and that the blood pressure is applied normal to each layer, the elastic modulus $E_{\theta,i}(l)$ of the i-th layer along the l-th beam is approximately given by[21]
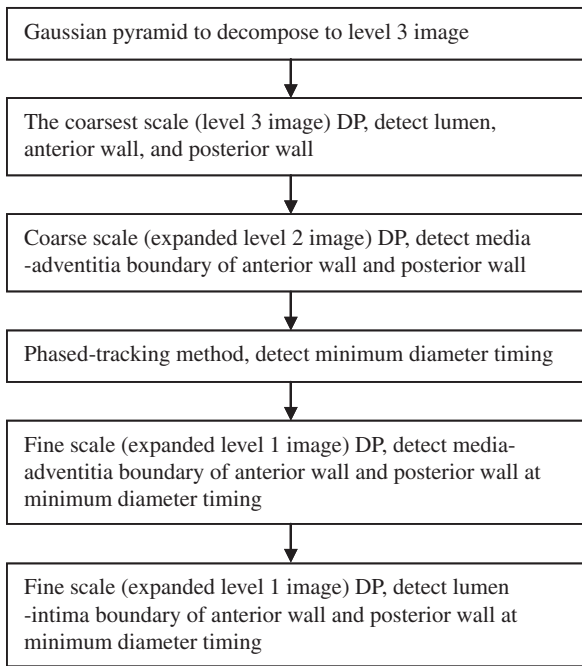
```
┌─────────────────────────────────────────────┐
│ Gaussian pyramid to decompose to level 3 image │
└─────────────────────────────────────────────┘
                      │
                      ▼
┌─────────────────────────────────────────────┐
│ The coarsest scale (level 3 image) DP, detect lumen, │
│ anterior wall, and posterior wall             │
└─────────────────────────────────────────────┘
                      │
                      ▼
┌─────────────────────────────────────────────┐
│ Coarse scale (expanded level 2 image) DP, detect media │
│ -adventitia boundary of anterior wall and posterior wall │
└─────────────────────────────────────────────┘
                      │
                      ▼
┌─────────────────────────────────────────────┐
│ Phased-tracking method, detect minimum diameter timing │
└─────────────────────────────────────────────┘
                      │
                      ▼
┌─────────────────────────────────────────────┐
│ Fine scale (expanded level 1 image) DP, detect media- │
│ adventitia boundary of anterior wall and posterior wall at │
│ minimum diameter timing                       │
└─────────────────────────────────────────────┘
                      │
                      ▼
┌─────────────────────────────────────────────┐
│ Fine scale (expanded level 1 image) DP, detect lumen │
│ -intima boundary of anterior wall and posterior wall at │
│ minimum diameter timing                       │
└─────────────────────────────────────────────┘
```

Fig. 3. Outline of automated detection procedure.

$$E_{\theta,i}(l) = \frac{3}{8}\left[1 + \frac{2\rho_{i0}(l)}{h_0(l)}\right]\frac{\Delta p}{\Delta \varepsilon_{i,\max}(l)}, \qquad (4)$$

where $\rho_{i0}(l)$ and Δp are the initial inner radius of curvature of the i-th layer along the l-th beam at a time t_0 of the minimum diameter and the pulse pressure (difference between the systolic blood pressure and the diastolic blood pressure) measured at the upper arm, respectively. The image of the regional elasticity of the posterior wall is obtained, as shown in Fig. 2(c). We have mostly focused on the regional elasticity of the posterior wall in our series of studies because it is often difficult to measure the regional elasticity of the anterior wall on clinical images because of multi-reflection artifacts and sidelobe artifacts. As described above, the lumen–intima and media–adventitia boundaries of the anterior and posterior walls must be determined for measurement of the elasticity of the posterior wall by this method.

2.2 Automated artery boundary detection method

The multiscale DP algorithm[36] is a technique for finding the boundaries by maximizing a certain cost function using multiscale images. In the present study, by applying this technique to pre-scan-converted B-mode images, which are constructed from the amplitude of the quadrature demodulated signal, the boundaries are detected. The reasons why we use pre-scan-converted B-mode images are as follows: introducing the correlation term between ultrasonic echoes in adjacent receive scan lines and reduction in computational load owing to reduction in image size. In a pre-scan-converted B-mode image, the pixel spacing is 0.12 mm/pixel in the lateral direction and 0.035 mm/pixel in the axial direction. An outline of the automated detection procedure is shown in Fig. 3.

2.2.1 Multiscale image
Firstly, we use a Gaussian pyramid to decompose an ultrasound image into multiscale images where a 5×5 Gaussian filter with the standard
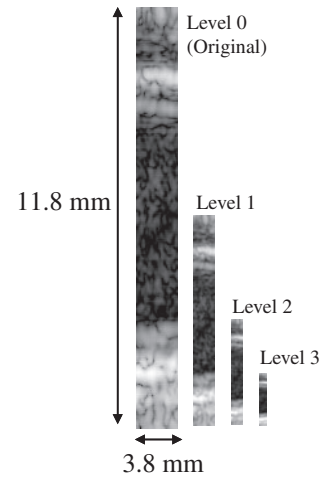

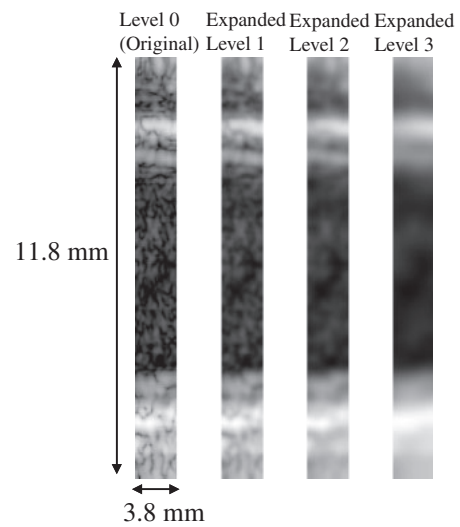**Fig. 4.** Gaussian pyramid images.

Fig. 5. Levels of Gaussian pyramid expanded to size of original image.

deviation σ of 1 for normalized envelope signals is used for smoothing.[42] In the level 1 image, the standard deviation σ of 1 and kernel size of 5 pixels in the axial direction were chosen to remove small noise and to detect the boundaries with a high degree of accuracy and preserve the shape of an ultrasound pulse, corresponding to approximately 10 pixels. The kernel size in the lateral direction is longer than that in the axial direction because a horizontally longer kernel makes it easier to detect arterial wall boundaries, which are a multilayer structure and often horizontally continuous. The original image is repeatedly filtered and subsampled to generate the sequence of reduced resolution images. The Gaussian pyramid images are shown in Fig. 4 and the levels of the Gaussian pyramid expanded to the size of the original image are shown in Fig. 5.

2.2.2 Cost function and dynamic programming
In a grid of image $M \times N$, consider a deformable polyline vector **b** containing N nodes, one in each column composed of M boundary candidates:

$$b = (b_1, b_2, \ldots, b_{i-1}, b_i, \ldots, b_N), \qquad (5)$$

where b_{i-1} and b_i are the horizontal neighboring points. At point b_i, a local cost $C(b_i)$ is defined by
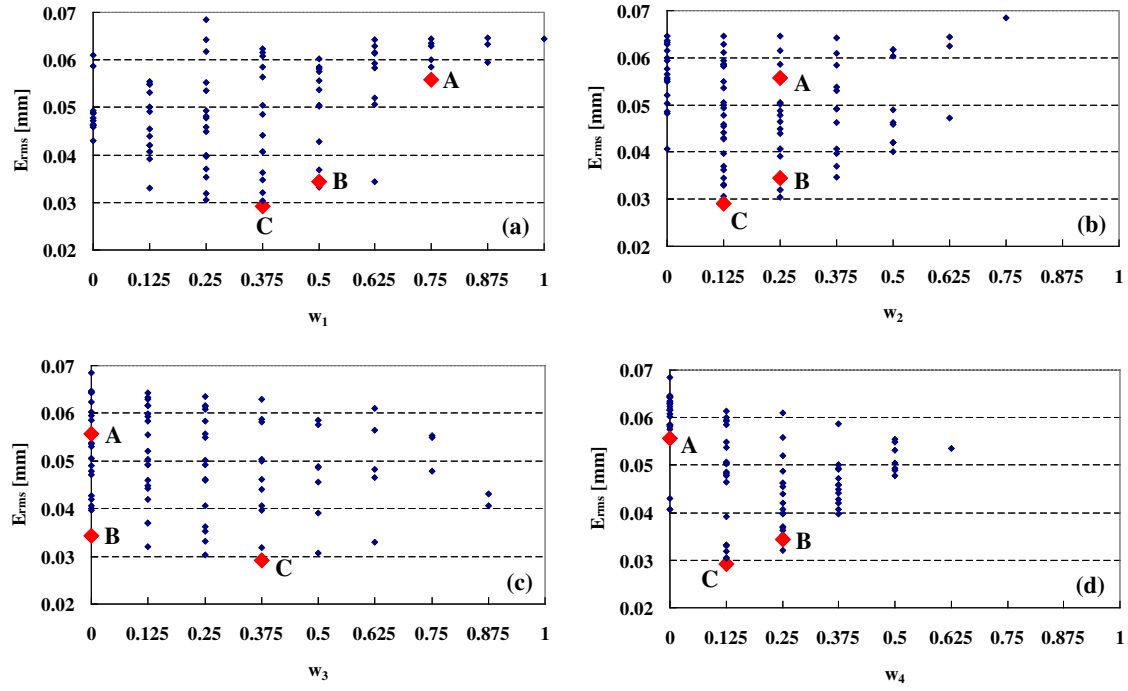
Fig. 6. (Color online) Averaged RMS error. (a) Projection of RMS error onto w_1 axis. (b) Projection of RMS error onto w_2 axis. (c) Projection of RMS error onto w_3 axis. (d) Projection of RMS error onto w_4 axis.

$$C(b_i) = w_1 I(b_i) + w_2 G(b_i) + w_3 R(b_{i-1}, b_i)$$
$$+ w_4 D(|b_{i-1} - b_i|), \qquad (6)$$

where I, G, R, and D are the cost function terms, which represent respective boundary features, and w_1, w_2, w_3, and w_4 are their weight factors, which reflect the relative importance of each boundary feature in each image level. Term I represents the echo intensity feature, which is a normalized differential value between the sum intensity of pixels below the interface and the sum intensity of pixels above the interface. The term G represents the echo intensity gradient feature, which is the normalized value of the downward intensity slope. The term R represents the lateral similarity to the feature in shape around the boundary. In the present study, R is employed as the cross correlation coefficient of ultrasonic signals around b_{i-1} and b_i. The cross correlation window length is almost equal to the pulse length. The term D is the vertical position continuity of the boundary, which prefers a smoother line,

$$D(|b_{i-1} - b_i|) = \begin{cases} -\dfrac{|b_{i-1} - b_i|}{L} & \text{for } |b_{i-1} - b_i| \leqq L \\ -\infty & \text{for } |b_{i-1} - b_i| > L \end{cases}, \quad (7)$$

where L is the supposed maximum change in the vertical distance between the adjacent lines and is set to 5 pixels (0.175 mm) here to detect a relatively sharp change in the vertical distance of lesions such as plaques. The relationship among the terms I, G, R, and D and the effect of the term R are explained in Sect. 2.2.4.

The cost function is defined as the sum of local costs along the polyline.

$$C_{\text{sum}} = \sum_{i=1}^{N} C(b_i). \qquad (8)$$

The optimum boundary is searched to maximize the cost

function C_{sum}. An exhaustive whole space $M \times N$ search needs a computational complexity $\mathbf{O}(M^N)$, which requires numerous calculations and could need a longer time than manual tracing. To reduce calculation time significantly, we search the optimum boundary by applying the DP procedure, and the computational complexity is reduced to $\mathbf{O}(N \times M^2)$.[35,43,44]

2.2.3 *Determining the weight factors* In this study, 20 subject images were analyzed. One-half of the images were used as training data for determining the weight factors in this section, the other half of the images were analyzed in Sect. 3.2. The cost function for detecting one interface includes four terms. Because we use the constraint $w_1 + w_2 + w_3 + w_4 = 1$, we only determine three of them. The combinations of (w_1, w_2, w_3), in steps of 1/8, such that $w_1 + w_2 + w_3 \leq 1$, have 165 patterns. For the values of (w_1, w_2, w_3), we apply the DP procedure to the training data and compute the root mean square (RMS) error between the automatically and manually assigned boundaries by a professional expert. The RMS error e_{RMS} is defined by the depth $d_{\text{auto}}(l)$ and $d_{\text{man}}(l)$ of the automatically detected boundary and manually assigned boundary at the beam position l as follows:

$$e_{\text{RMS}} = \sqrt{\frac{1}{N_b} \sum_{l=1}^{N_b} |d_{\text{auto}}(l) - d_{\text{man}}(l)|^2}, \qquad (9)$$

where N_b is the number of beam positions. The values of (w_1, w_2, w_3, w_4) associated with the lowest RMS error for each boundary are determined as the weight factors. As an example, we present the relationships between average RMS error among the 10 training images and the values of (w_1, w_2, w_3, w_4) for the media–adventitia boundary of the posterior wall of the expanded level 1 image in Fig. 6.
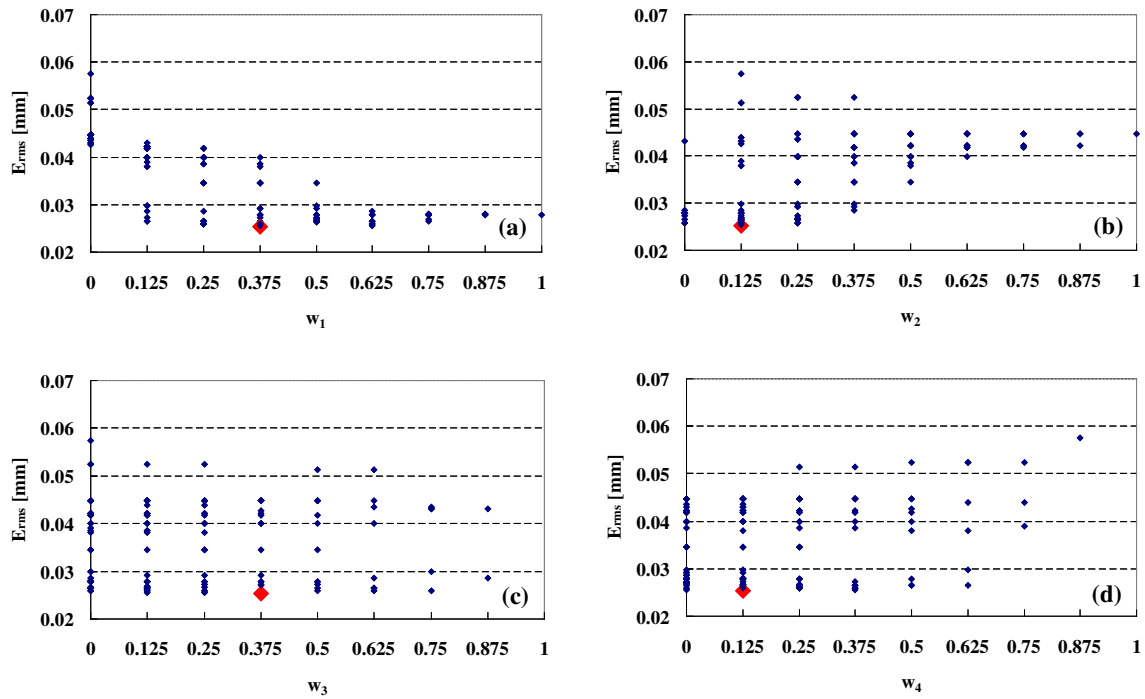
Fig. 7. (Color online) RMS error for image without speckle noise, in which boundaries are clearly seen. Data with minimum RMS errors are indicated by red diamonds. (a) Projection of RMS error onto w_1 axis. (b) Projection of RMS error onto w_2 axis. (c) Projection of RMS error onto w_3 axis. (d) Projection of RMS error onto w_4 axis.
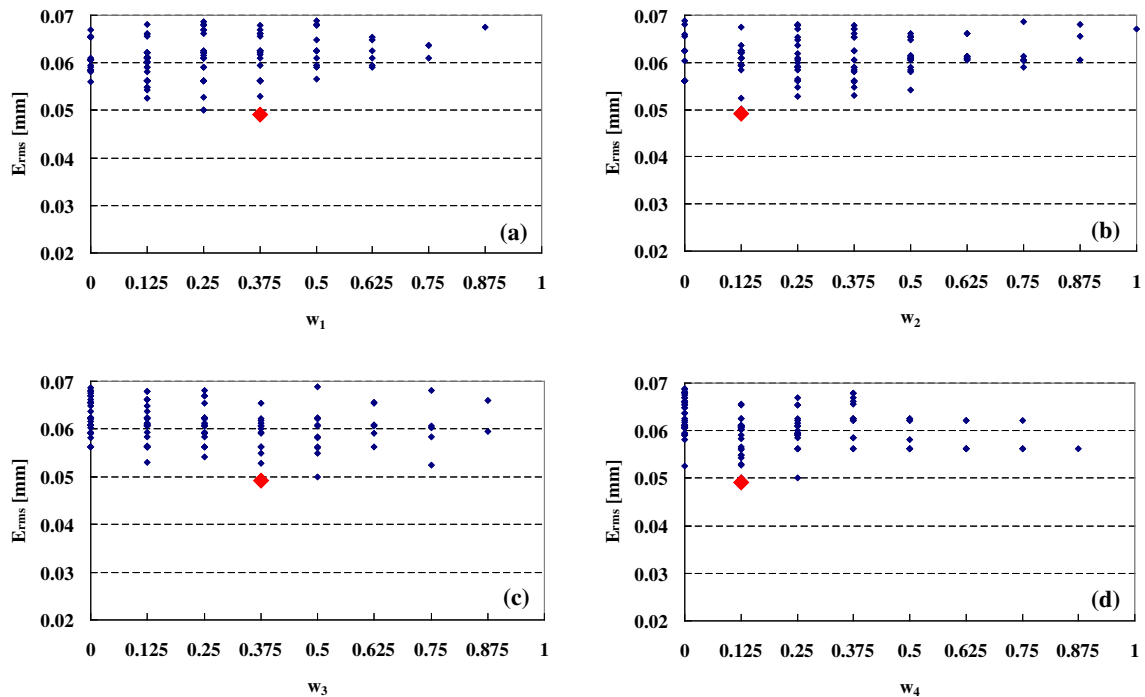

Fig. 8. (Color online) RMS error for image with speckle noise, in which boundaries are partly unclear. Data with minimum RMS errors are indicated by red diamonds. (a) Projection of RMS error onto w_1 axis. (b) Projection of RMS error onto w_2 axis. (c) Projection of RMS error onto w_3 axis. (d) Projection of RMS error onto w_4 axis.

Figures 6(a)–6(d) show the projection of e_{RMS} onto the w_1, w_2, w_3, and w_4 axes respectively. The e_{RMS} axis is zoomed around the minimum values. e_{RMS} is minimum when w_1, w_2, w_3, and w_4 are non-zero values. This suggests that it is better to consider all the terms I, G, D, and R. The values of (w_1, w_2, w_3, w_4) associated with the lowest RMS error were $(0.375, 0.125, 0.375, 0.125)$ and these weight factors were

used for the media–adventitia boundary of the posterior wall in the analysis in Sect. 3.2.

To investigate the tendencies of e_{RMS} and the weight factors, the projection results of e_{RMS} onto w_1, w_2, w_3, and w_4 of two subjects are shown in Figs. 7 and 8. Figure 7 is for a clear boundary image without speckle noise and Fig. 8 is for a partly unclear boundary image with speckle noise.
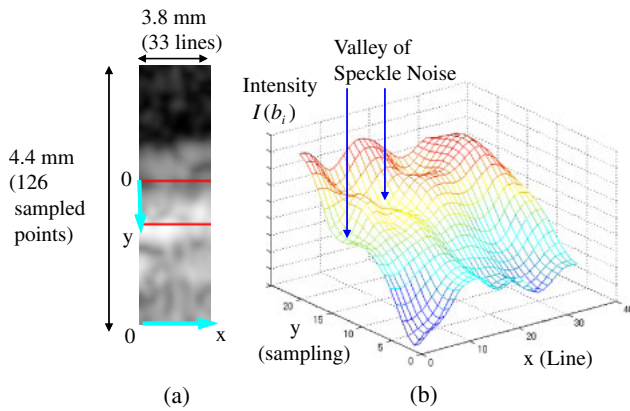
Fig. 9. (Color online) (a) Zoomed level 1 image of posterior wall. (b) 3D plot of level 1 image intensity around posterior media–adventitia boundary.
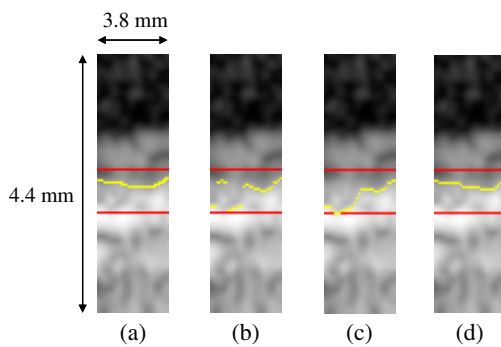

Fig. 10. (Color online) Manually traced and automatically detected boundary. (a) Boundary manually traced by a professional expert. (b) Automatically detected boundary considering only terms I and G calculated using values of point A. (c) Automatically detected boundary considering terms I, G, and D calculated using values of point B. (d) Boundary automatically detected by our method considering terms I, G, D, and R calculated by using values of point C.

In both figures, e_{RMS} is minimum at weight factors of $(0.375, 0.125, 0.375, 0.125)$ plotted with red diamonds. The dependence of weight factors observed in Fig. 8 is stronger than that observed in Fig. 7.

2.2.4 Effect of the terms *I*, *G*, *D*, and *R* So far, we have described the DP method. Here, we explain the effect of the terms I, G, D, and R using Fig. 6. Point A is $(0.75, 0.25, 0, 0)$ of (w_1, w_2, w_3, w_4), which leads to the minimum e_{RMS} when w_3 and w_4 are zero. Point B is $(0.5, 0.25, 0, 0.25)$ of (w_1, w_2, w_3, w_4), which leads to the minimum e_{RMS} when w_3 is zero. Point C is $(0.375, 0.125, 0.375, 0.125)$ of (w_1, w_2, w_3, w_4), which leads to the minimum e_{RMS} in all combinations of (w_1, w_2, w_3, w_4).

We explain the reason why the values of point C give the minimum e_{RMS} using a typical image, where the detection result using values of point C leads to a much lower e_{RMS} than that using values of points A and B. Figures 9(a) and 9(b) show the zoomed level 1 image of the posterior wall and the three-dimensional (3D) plot of level 1 image intensity around the posterior media–adventitia boundary. As shown in Figs. 9(a) and 9(b), the valley of speckle noise exists around the left half 1–3 lines and 10–16 lines.

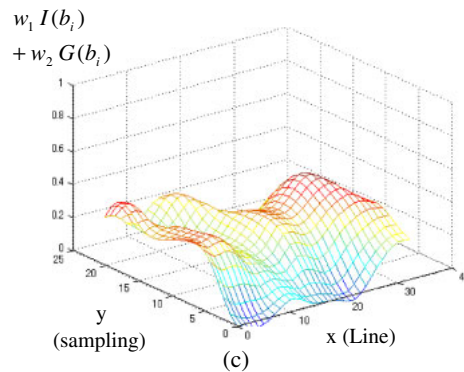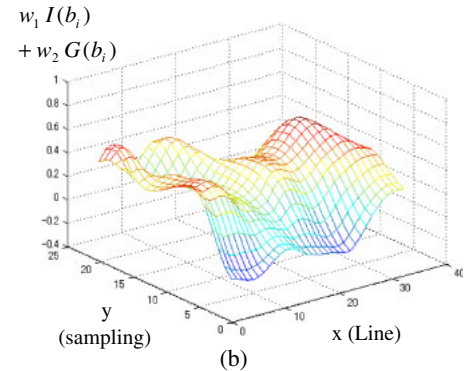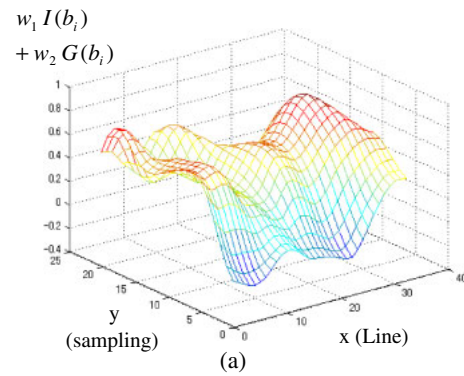Figure 10(a) shows the boundary manually traced by a professional expert. We can understand that the professional

Fig. 11. (Color online) 3D plot of $w_1 I + w_2 G$. (a) 3D plot of $w_1 I + w_2 G$ calculated using values of point A. (b) 3D plot of $w_1 I + w_2 G$ calculated using values of point B. (c) 3D plot of $w_1 I + w_2 G$ calculated using values of point C.

expert traces the boundary such that speckle noise edges are avoided and boundary continuity is given importance. Figure 10(b) shows the boundary automatically detected using the values of point A and Fig. 11(a) shows the 3D plot of $w_1 I + w_2 G$. The use of the values of point A detects speckle noise edges by mistake and leads to a higher e_{RMS}, 0.105 mm, because the intensity and gradient at the boundary with speckle noise are higher than those at the manually traced boundary. Because the values of point A, which are w_3 and w_4, are zero, the continuity of the boundary is not considered. Figure 10(c) shows the automatically detected boundary using values of point B, and Fig. 11(b) shows the 3D plot of $w_1 I + w_2 G$. The use of the values of point B also detects speckle noise edges by mistake and leads to a higher e_{RMS}, 0.135 mm. This is because the manually traced boundary indicates lower values of intensity and gradient than the speckle noise edges at the lines with speckle noise, and the speckle noise edge depth changes continuously, which means the change in the speckle noise edge depth
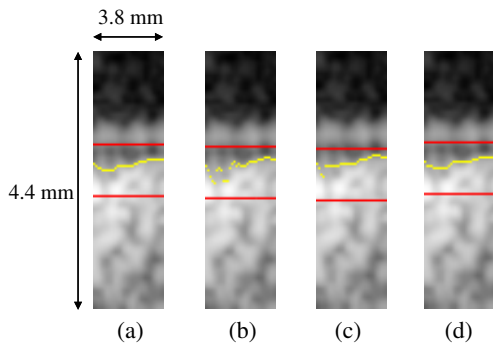
Fig. 12. (Color online) Manually traced and automatically detected boundaries for another subject. (a) Boundary manually traced by a professional expert. (b) Automatically detected boundary considering only terms I and G calculated using values of point A. (c) Automatically detected boundary considering terms I, G, and D calculated using values of point B. (d) Boundary automatically detected by our method considering terms I, G, D, and R calculated using values of point C.

Fig. 13. (Color online) 3D plot of $w_1 I + w_2 G$ for another subject. (a) 3D plot of $w_1 I + w_2 G$ calculated using values of point A. (b) 3D plot of $w_1 I + w_2 G$ calculated using values of point B. (c) 3D plot of $w_1 I + w_2 G$ calculated using values of point C.

between adjacent lines is small. Figure 10(d) shows the boundary automatically detected using the values of point C, and Fig. 11(c) shows the 3D plot of $w_1 I + w_2 G$. The use of the values of point C leads to a lower e_{RMS}, 0.028 mm, which is close to the manually traced result. As one more example, the manually traced and detection results of another subject are shown in Figs. 12(a)–12(d) and the 3D plots of $w_1 I + w_2 G$ are shown in Figs. 13(a)–13(c).

These results show that the term R, which represents the lateral similarity between the waveforms of ultrasonic echoes, is effective even in the boundary with speckle noise. This is because the lateral similarity between adjacent lines is conserved even in the boundary with speckle noise, as we can see in 1–3 lines and 10–16 lines in Fig. 9(b), although the intensity and gradient are relatively lower in the boundary with speckle noise. The results of detection using the values of points B and C indicate that a professional expert traces the boundary in terms of not only the continuity of the change in the vertical distance but also the continuity of the waveform especially in the boundary with speckle noise.

Regardless of whether the term R is used, detection results are similar at clear boundary lines without speckle noise such as 16–33 lines, because the intensity and gradient are higher. However, at boundary lines with speckle noise such as 10–16 lines, the intensity and gradient are lower and the speckle noise edge depth changes continuously; only the detection considering the term R shows results close to those in which the boundary is manually assigned.

2.2.5 Detection of the minimum diameter timing

To detect the minimum diameter timing at which precise boundary detection is conducted, firstly, we detect the lumen, anterior wall, and posterior wall roughly using the coarsest scale (level 3) image. In the level 3 image, the center depth of the lumen is easily determined as the depth where the mean intensity obtained by averaging the intensity profile laterally is minimum. The level 3 image is divided into the upper part and lower part at the depth of the centered lumen, and DP is conducted in the upper part to detect the anterior wall and in the lower part to detect the posterior wall. Figure 14(a) shows the level 3 image, and Fig. 14(b) shows the level 3 image with the automatically detected lumen, anterior, and posterior
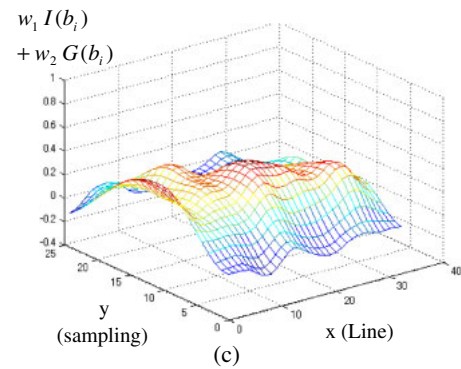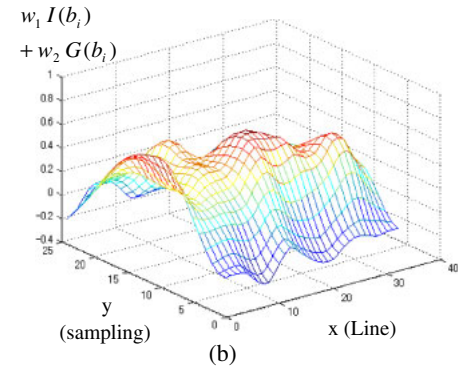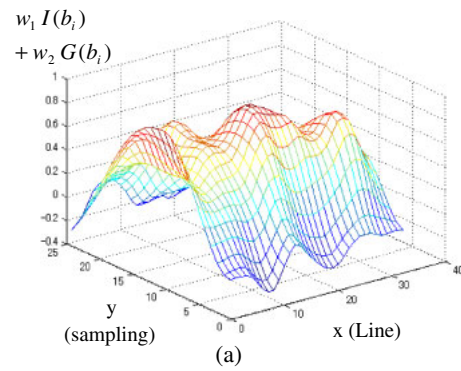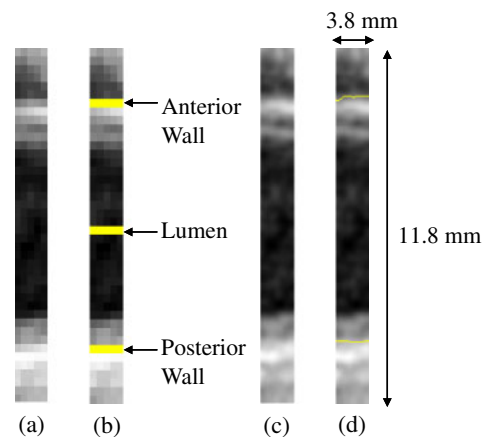

Fig. 14. (Color online) (a) Level 3 image. (b) Level 3 image with automatically detected lumen, anterior, and posterior wall boundaries overlaid. (c) Extended level 2 image. (d) Extended level 2 image with automatically detected anterior media–adventitia boundary and posterior–media adventitia boundary overlaid.
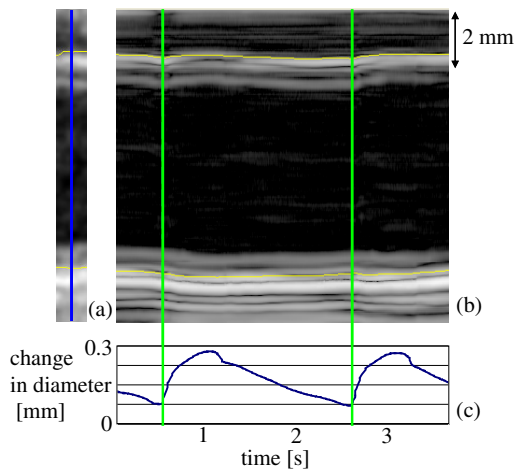
Fig. 15. (Color online) (a) Extended level 2 image with automatically detected anterior media–adventitia boundary and posterior media–adventitia boundary overlaid. (b) M-mode image in the red line in Fig. 11(a) with anterior and posterior wall media–adventitia boundary tracking results overlaid. (c) Change in vascular diameter.

Fig. 16. (Color online) (a) Expanded level 1 image at minimum diameter timing. (b) Expanded level 1 image with automatically detected anterior lumen–intima boundary, anterior media–adventitia boundary, posterior lumen–intima boundary, and posterior media–adventitia boundary at minimum diameter timing.

wall boundaries overlaid. Secondly, the media–adventitia boundary is detected because echoes from the media–adventitia boundary are larger and easier to detect than those from the lumen–intima boundary. The anterior media–adventitia boundary is detected in the expanded level 2 image by DP searching around the depth of the arterial wall detected in the level 3 image, and the posterior media–adventitia boundary is detected in the expanded level 2 image by DP searching around the depth of the posterior wall detected in the level 3 image. The DP searching range is within ± 1 mm from the depth of the detected boundary in level 3, because a typical gap between the coarsely and finely determined boundary positions is less than 0.35 mm of the ultrasonic pulse length. An expanded level 2 image is shown in Fig. 14(c) and an expanded level 2 image with the automatically detected anterior media–adventitia boundary and posterior media–adventitia boundary overlaid is shown in Fig. 14(d). Lastly, to detect the change in diameter and local minimum diameter timing, the phased-tracking method is applied to the quadrature demodulated signal from the depths of the detected anterior media–adventitia boundary and posterior media–adventitia boundary in the expanded level 2 image. Figure 15(a) shows the level 2 image with the automatically detected anterior media–adventitia boundary and posterior media adventitia boundary overlaid, and Fig. 15(b) shows the M-mode image in the red line in Fig. 15(a) with the anterior and posterior wall media–adventitia boundaries tracking results overlaid. The change in diameter estimated by the phased-tracking method is shown in Fig. 15(c). The local minimum diameter timings are indicated by the green lines in Figs. 15(b) and 15(c).

2.2.6 Boundary detection at minimum diameter timing

Using the expanded level 1 image at local minimum diameter timing, fine-scale DP detection of the anterior media–adventitia boundary, anterior lumen–intima boundary, posterior media–adventitia boundary, and posterior lumen–intima boundary is conducted. Firstly, the media–adventitia boundary is detected on the basis of the boundary positions detected in a coarser scale (expanded level 2) image.
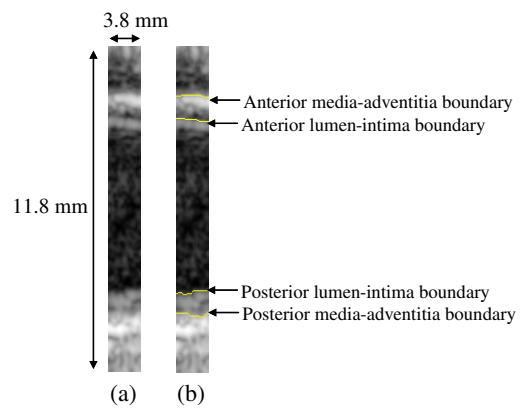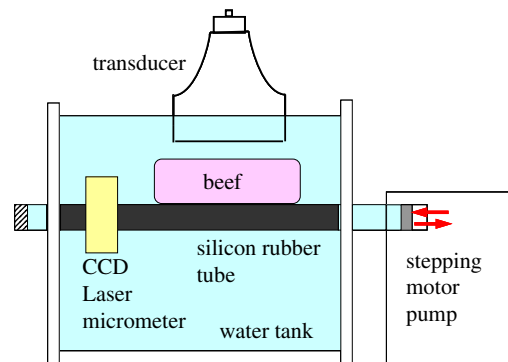

Fig. 17. (Color online) Arterial-wall-mimicking-phantom made of silicone rubber tube pulsated by stepping motor pump.

Subsequently, the lumen–intima boundary is detected by searching 2.5 mm inside the media–adventitia boundary position detected. The search range of 2.5 mm is chosen to cover a typical intima–media thickness, which is less than 2 mm. The expanded level 1 image is shown in Fig. 16(a), and the expanded level 1 image with the automatically detected anterior lumen–intima boundary, anterior media–adventitia boundary, posterior lumen–intima boundary, and posterior media–adventitia boundary is shown in Fig. 16(b).

3. Results

3.1 Basic experiments using silicone tube phantom

To evaluate the accuracy of the detected minimum diameter timing and boundaries, we prepared a phantom mimicking the arterial wall made of a silicone rubber tube, which was pulsated by a stepping motor pump, as shown in Fig. 17. The thickness of the silicone rubber tube is 1.1 mm and the inner diameter is 8 mm, which are similar to those of the carotid artery. The material of the silicone rubber tube includes graphite powder (weight ratio, 5%), acting as ultrasound scatters. To evaluate the change in external diameter by a method other than the proposed method, a CCD laser micrometer (Keyence IG-028) is located across a transparent water tank. To mimic random speckle noise in the B-mode used in clinical settings, a thick piece of beef was located on the silicone rubber tube.
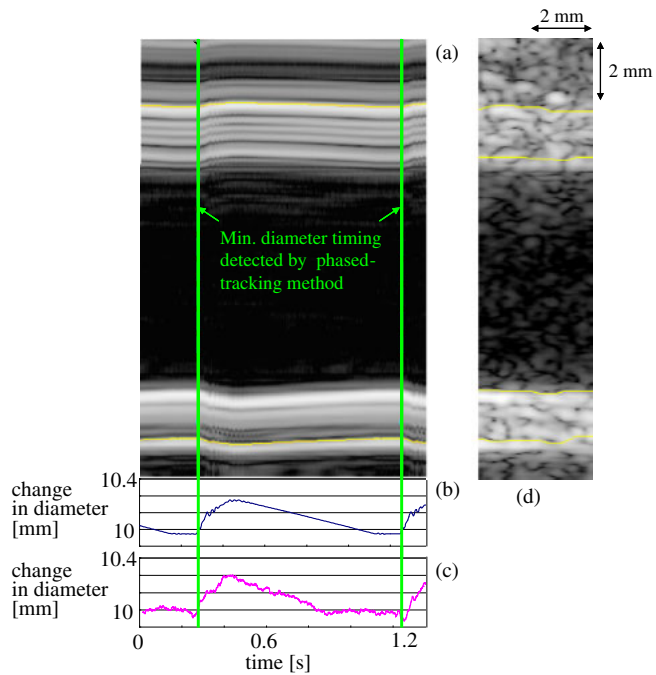
Fig. 18. (Color online) (a) Arterial-wall-mimicking-phantom M-mode image with anterior and posterior wall media–adventitia boundary tracking results overlaid. (b) Change in diameter measured by phased-tracking method. (c) Change in diameter measured using CCD laser micrometer. (d) Arterial-wall-mimicking-phantom B-mode image with automatically detected anterior lumen–intima boundary, anterior media–adventitia boundary, posterior lumen–intima boundary, and posterior media adventitia boundary.

Fig. 19. (Color online) (a) Scan-converted B-mode image of arterial-wall-mimicking phantom at minimum diameter timing. (b) Scan-converted B-mode image with automatically detected boundaries considering only terms *I* and *G* overlaid. (c) Scan-converted B-mode image with automatically detected boundaries considering terms *I*, *G*, and *D* overlaid. (d) Scan-converted B-mode image with automatically detected boundaries considering terms *I*, *G*, *D*, and *R* overlaid.

Figures 18(a)–18(c) show M-mode images with the tracking results with respect to the anterior and posterior wall media–adventitia boundaries overlaid, the change in diameter measured by the phased-tracking method, and the change in diameter measured by the CCD laser micrometer, respectively. The diameter was calculated by the phased-tracking method considering a sound speed of 1030 m/s for the silicone rubber tube and that of 1480 m/s for water. Figure 18(d) shows a scan-converted B-mode image with the automatically detected anterior lumen–intima boundary, anterior media–adventitia boundary, posterior lumen–intima boundary, and posterior media adventitia boundary. Comparing Fig. 18(b) with Fig. 18(c), the difference in minimum diameter timings between the phased-tracking method and the method using a CCD laser micrometer is less than 0.015 s. Figures 19(a)–19(d) show a scan-converted B-mode image, a scan-converted B-mode image with automatically detected boundaries considering only terms *I* and *G* overlaid, a scan-converted B-mode image with the automatically detected boundaries considering terms *I*, *G*, and *D* overlaid, and a scan-converted B-mode image with the automatically detected boundaries considering terms *I*, *G*, *D*, and *R* overlaid at the minimum diameter timing, respectively. The average and maximum thicknesses of the silicone rubber tube are calculated considering a sound of 1030 m/s for the silicone rubber tube. The average thicknesses of the anterior wall are 1.18 mm in Fig. 19(b), 1.09 mm in Fig. 19(c), and 1.09 mm in Fig. 19(d). Also, the average thicknesses of the posterior wall are 1.05 mm in Fig. 19(b), 1.04 mm in Fig. 19(c), and 1.06 mm in Fig. 19(d). The maximum thicknesses of the anterior wall are 1.44 mm in Fig. 19(b), 1.37 mm in
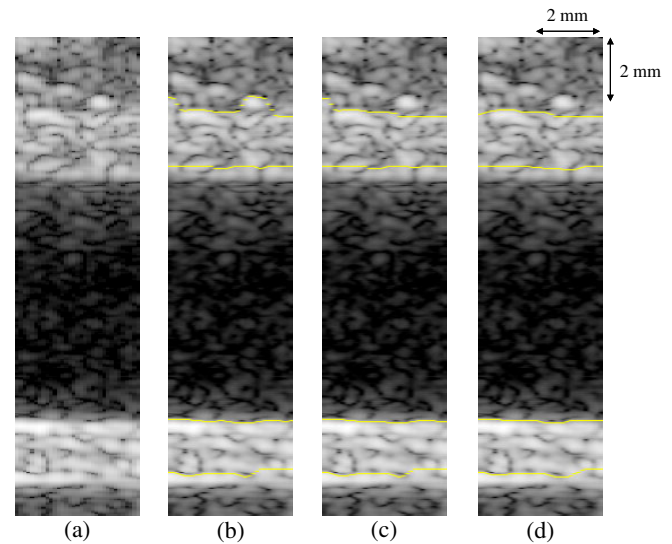
Fig. 19(c), and 1.12 mm in Fig. 19(d). The maximum thicknesses of the posterior wall are 1.14 mm in Fig. 19(b), 1.14 mm in Fig. 19(c), and 1.14 mm in Fig. 19(d). The thickness of the silicone rubber tube is measured to be 1.1 mm under a microscope and the surface is confirmed to be flat; the estimated maximum thicknesses of the anterior wall in Figs. 19(b) and 19(c) have a margin of error. On the other hand, the estimated average and maximum thicknesses in Fig. 19(d) are well in agreement with the results of measurement under a microscope.

3.2   In vivo experimental results for human carotid artery

The proposed method was applied to the in vivo measurement of carotid arteries, and the root mean square errors between the proposed method, and the manual assignment of the boundaries were evaluated in 10 subjects with and without atherosclerotic plaques. Examples of images of a subject without atherosclerotic plaques are shown in Fig. 20 and those of a subject with atherosclerotic plaques are shown in Fig. 21. In both figures, (a), (b), (c), (d), and (e) show a scan-converted B-mode image, a scan-converted B-mode image with the automatically detected boundaries considering only terms *I* and *G* overlaid, a scan-converted B-mode image with the automatically detected boundaries considering terms *I*, *G*, and *D* overlaid, a scan-converted B-mode image with the automatically detected boundaries considering terms *I*, *G*, *D*, and *R* overlaid, and a scan-converted B-mode image with the boundaries manually traced by a professional expert at the minimum diameter timing, respectively. In Fig. 20, the relatively clear boundaries, anterior media–adventitia boundary, anterior lumen–intima boundary, and posterior lumen–intima boundary, are very close to the manually assigned boundaries for all automated detection methods. On the other hand, for the posterior media–adventitia boundary, in which speckle noise is present, only the proposed method is in good agreement
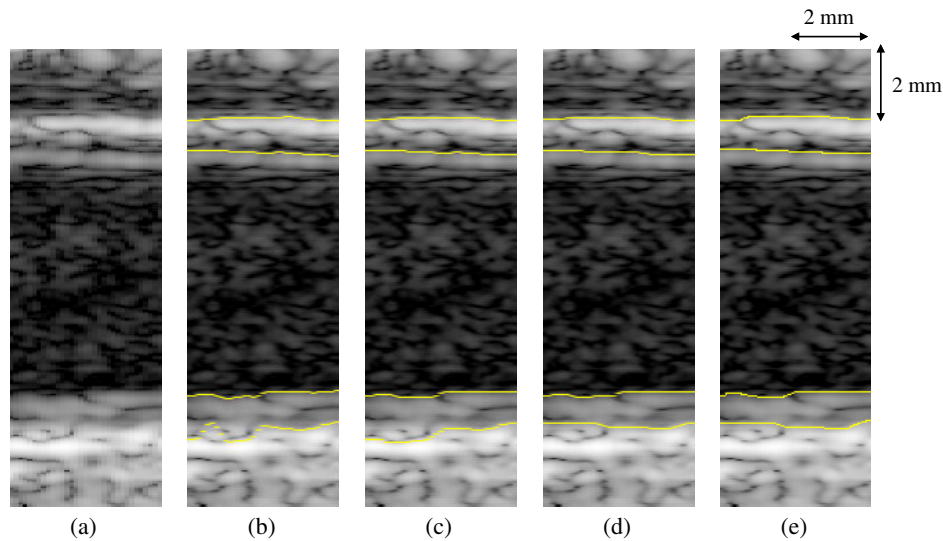
Fig. 20. (Color online) Examples of images of subject without plaques. (a) Scan-converted B-mode image. (b) Scan-converted B-mode image with automatically detected boundaries considering only terms *I* and *G* overlaid. (c) Scan-converted B-mode image with automatically detected boundaries considering terms *I*, *G*, and *D* overlaid. (d) Scan-converted B-mode image with automatically detected boundaries considering terms *I*, *G*, *D*, and *R* overlaid. (e) Scan-converted B-mode image with the boundaries manually traced by a professional expert.
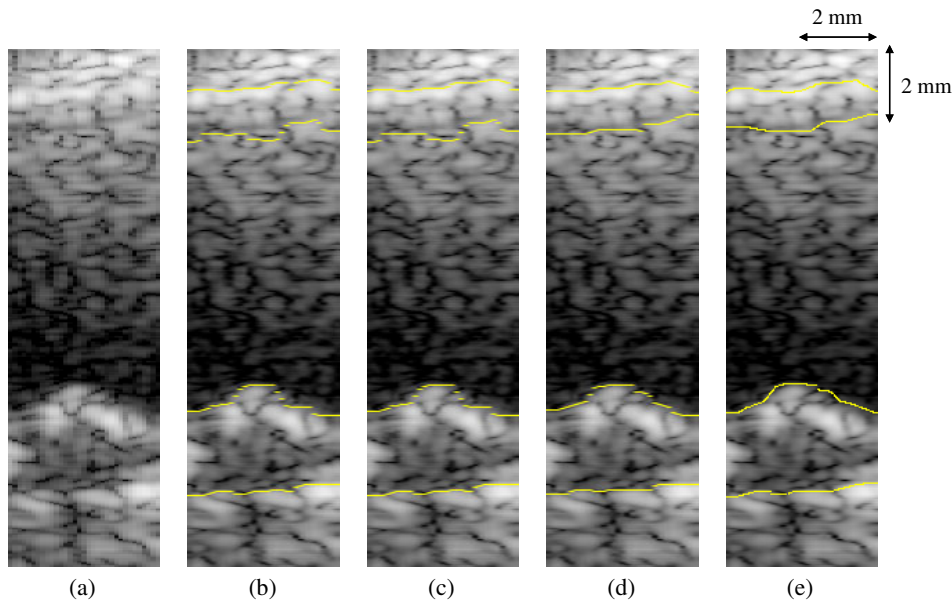

Fig. 21. (Color online) Examples of images of a subject with plaques. (a) Scan-converted B-mode image. (b) Scan-converted B-mode image with automatically detected boundaries considering only terms *I* and *G* overlaid. (c) Scan-converted B-mode image with automatically detected boundaries considering terms *I*, *G*, and *D* overlaid. (d) Scan-converted B-mode image with automatically detected boundaries considering terms *I*, *G*, *D*, and *R* overlaid. (e) Scan-converted B-mode image with the boundaries manually traced by a professional expert.

with the manually traced boundaries. In Fig. 21, the proposed method shows a smoother plaque boundary, which is closer to the manual tracing than the other methods. In 10 subjects, the root mean square errors between all methods and the manual assignment are 0.069 mm for the method considering only terms *I* and *G*, 0.050 mm for the method considering terms *I*, *G*, and *D*, and 0.034 mm for the proposed method considering terms *I*, *G*, *D*, and *R*. Compared with the other methods, the proposed method indicates smaller root mean square errors.

4. Discussion

In conventional arterial wall boundary detection procedures, intensity and its gradient terms of each scan line are used.

Although such simple methods lead to precise detection if a B-mode image is clear, they are not sufficient for most B-mode images in clinical settings because they contain various types of noise such as speckle noise. Therefore, several methods using cost function have been proposed for robust noise detection of the boundaries. Liang et al. proposed a fully automated method using multiscale DP, in which the cost function is composed of echo intensity, echo intensity gradient, and change in vertical distance.[36] However, this method is also insufficient to balance strong speckle noises with abrupt boundary changes in the vertical distance in cases such as plaques. As shown in Sect. 3, adding the viewpoint of lateral similarity feature with respect to waveforms of ultrasonic echoes to cost function enables the balance

between noise robustness and detection of the abrupt change in the boundary. It is important and effective to consider not only the continuity in the vertical position but also the lateral continuity with respect to waveforms of ultrasonic echoes for the boundary detection.

5. Conclusions

We have proposed an automated arterial wall boundary detection method using multiscale DP, in which the cost function includes the correlation term between ultrasonic echoes in adjacent receive scan lines. The accuracy of the proposed method was validated using a phantom mimicking the arterial wall made of a silicone rubber tube pulsated by a stepping motor pump. The proposed method was also applied to the in vivo measurement of carotid arteries, and the results were compared with results manually traced by a human expert. The proposed method was much closer to the results obtained by a human expert than to the results of the simple method using only intensity and its gradient in each scan line and the DP method using only the change in vertical distance in successive scan line. The correlation term enables boundary detection to be more robust against noises. The proposed method shows potential for detecting arterial wall boundaries automatically and may be useful for elasticity imaging.

1) H. Tanaka, M. Nishino, M. Ishida, R. Fukunaga, and K. J. Sueyoshi, Stroke **23**, 946 (1992).
2) R. T. Lee, A. J. Grodzinsky, E. H. Frank, R. D. Kamm, and F. J. Schoen, Circulation **83**, 1764 (1991).
3) H. M. Loree, A. J. Grodzinsky, S. Y. Park, L. J. Gibson, and R. T. Lee, J. Biomech. **27**, 195 (1994).
4) P. C. G. Simons, A. Algra, M. L. Bots, D. E. Grobbee, and Y. van der Graaf, Circulation **100**, 951 (1999).
5) J. T. Salonen and R. Salonen, Circulation **87**, 1156 (1993).
6) P. Pignoli, E. Tremoli, A. Poli, P. Oreste, and R. Paoletti, Circulation **74**, 1399 (1986).
7) E. de Groot, G. K. Hovingh, A. Wiegman, P. Duriez, A. J. Smit, J.-C. Fruchart, and J. J. P. Kastelein, Circulation **109**, III-33 (2004).
8) S. Kageyama, H. Hasegawa, and H. Kanai, Jpn. J. Appl. Phys. **52**, 07HF04 (2013).
9) C. Arihara, H. Hasegawa, and H. Kanai, Jpn. J. Appl. Phys. **45**, 4727 (2006).
10) T. Kaneko, H. Hasegawa, and H. Kanaii, Jpn. J. Appl. Phys. **46**, 4881 (2007).
11) K. Kitamura, H. Hasegawa, and H. Kanai, Jpn. J. Appl. Phys. **51**, 07GF08 (2012).
12) Y. Nagai, H. Hasegawa, and H. Kanai, Jpn. J. Appl. Phys. **53**, 07KF19 (2014).
13) J. Blacher, R. Asmar, S. Djane, G. M. London, and M. E. Safar, Hypertension **33**, 1111 (1999).
14) P. Hallock, Arch. Int. Med. **54**, 770 (1934).
15) M. Saito, Y. Yamamoto, Y. Shibayama, M. Matsukawa, Y. Watanabe, M. Furuya, and T. Asada, Jpn. J. Appl. Phys. **50**, 07HF10 (2011).
16) H. Kanai, H. Hasegawa, N. Chubachi, Y. Koiwa, and M. Tanaka, IEEE Trans. Ultrason. Ferroelectr. Freq. Control **43**, 791 (1996).
17) H. Hasegawa, H. Kanai, N. Hoshimiya, N. Chubachi, and Y. Koiwa, Jpn. J. Appl. Phys. **37**, 3101 (1998).
18) H. Hasegawa, H. Kanai, N. Hoshimiya, and Y. Koiwa, Jpn. J. Appl. Phys. **39**, 3257 (2000).
19) H. Hasegawa, H. Kanai, and Y. Koiwa, Jpn. J. Appl. Phys. **41**, 3563 (2002).
20) H. Hasegawa, H. Kanai, N. Chubachi, and Y. Koiwa, J. Acoust. Soc. Jpn. **53**, 346 (1997) [in Japanese].
21) M. Cinthio, H. Hasegawa, and H. Kanai, Proc. IEEE Int. Ultrasonics Symp., 2007, p. 997.
22) H. Hasegawa and H. Kanai, Jpn. J. Appl. Phys. **43**, 3197 (2004).
23) J. Inagaki, H. Hasegawa, H. Kanai, M. Ichiki, and F. Tezuka, Jpn. J. Appl. Phys. **44**, 4593 (2005).
24) J. Tang, H. Hasegawa, and H. Kanai, Jpn. J. Appl. Phys. **44**, 4588 (2005).
25) K. Ikeshita, H. Hasegawa, and H. Kanai, Jpn. J. Appl. Phys. **47**, 4165 (2008).
26) K. Ikeshita, H. Hasegawa, and H. Kanai, Jpn. J. Appl. Phys. **48**, 07GJ10 (2009).
27) K. Ikeshita, H. Hasegawa, and H. Kanai, Jpn. J. Appl. Phys. **50**, 07HF08 (2011).
28) K. Ikeshita, H. Hasegawa, and H. Kanai, Jpn. J. Appl. Phys. **51**, 07GF14 (2012).
29) M. Sato, H. Hasegawa, and H. Kanai, Jpn. J. Appl. Phys. **53**, 07KF03 (2014).
30) P.-J. Touboul, P. Prati, P.-Y. Scarabin, V. Adrai, E. Thibout, and P. Ducimetière, J. Hypertension **10**, 37 (1992).
31) J. Gariepy, M. Massonneau, J. Levenson, D. Heudes, and A. Simon, Hypertension **22**, 111 (1993).
32) R. H. Selzer, H. N. Hodis, H. Kwong-Fu, W. J. Mack, P. L. Lee, C. R. Liu, and C. H. Liu, Atherosclerosis **111**, 1 (1994).
33) F. Beux, S. Carmassi, M. V. Salvetti, L. Ghiadoni, Y. Huang, S. Taddei, and A. Salvetti, Ultrasound Med. Biol. **27**, 1621 (2001).
34) H. Hasegawa, H. Kanai, and Y. Koiwa, IEEE Trans. Ultrason. Ferroelectr. Freq. Control **51**, 93 (2004).
35) T. Gustavsson, Q. Liang, I. Wendelhag, and J. Wikstrand, Proc. IEEE Computers Cardiology, 1994, p. 297.
36) Q. Liang, I. Wendelhag, J. Wikstrand, and T. Gustavsson, IEEE Trans. Med. Imaging **19**, 127 (2000).
37) I. Wendelhag, Q. Liang, T. Gustavsson, and J. Wikstrand, Stroke **28**, 2195 (1997).
38) R. Rocha, A. Campilho, J. Silva, E. Azevedo, and R. Santos, Image Vision Comput. **28**, 614 (2010).
39) N. Ibrahim, H. Hasegawa, and H. Kanai, Jpn. J. Appl. Phys. **51**, 07GF07 (2012).
40) N. Ibrahim, H. Hasegawa, and H. Kanai, Jpn. J. Appl. Phys. **52**, 07HF03 (2013).
41) L. Y. L. Mo, D. DeBusschere, W. Bai, D. Napolitano, A. Irish, S. Marschall, G. W. McLaughlin, Z. Yang, P. L. Carson, and J. B. Fowlkes, Proc. IEEE Int. Ultrasonics Symp., 2007, p. 2259.
42) P. J. Burt and E. H. Adeloson, IEEE Trans. Commun. **31**, 532 (1983).
43) R. Bellman, *Dynamic Programming* (Princeton University Press, Princeton, NJ, 1962) p. 180.
44) H. Satoh, H. Kanai, and N. Chubachi, Nihon Onkyo Gakkaishi **50**, 11 (1994) [in Japanese].